

# Dynamic Crack Initiation And Growth In Cellulose Nanopaper

**Chengyun Miao**

Auburn University

**Haishun Du** (✉ [hzd0024@auburn.edu](mailto:hzd0024@auburn.edu))

Auburn University <https://orcid.org/0000-0002-8046-0319>

**Xinyu Zhang**

Auburn University

**Hareesh Tippur**

Auburn University

---

## Research Article

**Keywords:** Cellulose Nanopaper, Crack Initiation and Growth, Dynamic Fracture, Ultrahigh-speed photography, Digital Image Correlation

**Posted Date:** July 6th, 2021

**DOI:** <https://doi.org/10.21203/rs.3.rs-600089/v1>

**License:**   This work is licensed under a Creative Commons Attribution 4.0 International License.

[Read Full License](#)

---

**Version of Record:** A version of this preprint was published at Cellulose on November 22nd, 2021. See the published version at <https://doi.org/10.1007/s10570-021-04310-x>.

# DYNAMIC CRACK INITIATION AND GROWTH IN CELLULOSE NANOPAPER

Chengyun Miao • Haishun Du • Xinyu Zhang • Hareesh V. Tippur

Chengyun Miao (✉)

*Department of Mechanical Engineering, Auburn University, Auburn, AL, 36849, USA*

*Now at Hopkins Extreme Materials Institute, Johns Hopkins University, Baltimore, MD, 21218, USA*

E-mail: [czm0048@auburn.edu](mailto:czm0048@auburn.edu)

Haishun Du • Xinyu Zhang

*Department of Chemical Engineering, Auburn University, Auburn, AL, 36849, USA*

Hareesh V. Tippur

*Department of Mechanical Engineering, Auburn University, Auburn, AL, 36849, USA*

## Abstract

Cellulose nanopaper (CNP) made of cellulose nanofibrils (CNF) has gained extensive attention in recent years for its lightweight and superior mechanical properties alongside sustainable and green attributes. The mechanical characterization studies on CNP at the moment have generally been limited to tension tests. In fact, thus far there has not been any report on crack initiation and growth behavior, especially under dynamic loading conditions. In this work, crack initiation and growth in self-assembled CNP, made from filtration of CNF suspension, are studied using a full-field optical method. Dynamic crack initiation and growth behaviors and time-resolved fracture parameters are quantified using Digital Image Correlation (DIC) technique. The challenge associated with dynamic loading of a thin strip of CNP has been overcome by an acrylic holder with a wide pre-cut slot bridged by edge-cracked CNP. The ultrahigh-speed digital photography is implemented to map in-plane deformations during pre- and post-crack initiation regimes including dynamic crack growth. Under stress wave loading conditions, macroscale crack growth occurs at surprisingly high-speed (600-700 m/s) in this microscopically fibrous material. The measured displacement fields from dynamic loading conditions are analyzed to extract stress intensity factors (SIF) and energy release rate ( $G$ ) histories. The results show that the SIF at crack initiation is in the range of 6-7 MPa(m)<sup>1/2</sup>, far superior to many engineering plastics. Furthermore, the measured values increase during crack propagation under both low- and high-strain rates, demonstrating superior fracture resistance of CNP valuable for many structural applications.

34 **Keywords** Cellulose Nanopaper; Crack Initiation and Growth; Dynamic Fracture; Ultrahigh-  
35 speed photography; Digital Image Correlation.

## 36 **1. Introduction**

37 Cellulose nanofibrils (CNF), an advanced bio-nano-material produced from lignocellulosic  
38 biomass, offers outstanding properties such as high elastic modulus, high specific surface area,  
39 high thermal stability, as well as biocompatibility, biodegradability and lightweight characteristics  
40 (Du et al., 2020; Xie et al., 2018). Therefore, CNFs possess great engineering potential in the fields  
41 of biomedical implants (Du et al., 2019; Liu et al., 2020) and reinforcing nanofillers for structural  
42 composites (Chen et al., 2020; Kargarzadeh et al., 2018; K. Y. Lee et al., 2014). Due to large  
43 specific surface area, high aspect ratio and semi-crystalline structure, CNFs exhibit remarkable  
44 tendency to entangle and form flexible and mechanically stable film or sheet, often referred to as  
45 cellulose nanopaper (CNP) (Benítez & Walther, 2017). In addition to excellent mechanical  
46 properties, CNP also offer high thermal durability, tunable optical properties, as well as low  
47 thermal expansion coefficient (Wang et al., 2018). These make it a promising lightweight material  
48 for various multifunctional and high-end applications such as visual display substrates (Jung et al.,  
49 2015), organic solar cells (Nogi et al., 2015), and electrodes for energy storage (Xing et al., 2019).

50 A few results on the fracture behavior of CNP are reported in recent years. Zhu et al. (Zhu  
51 et al., 2015) found that the crack initiation toughness of CNP increased with the tensile strength.  
52 Using atomistic simulation, they attributed this to breaking and re-formation of hydrogen bonds  
53 among CNFs at crack initiation. Mao et al. (Mao et al., 2017) performed a comparative  
54 investigation of the fracture mechanisms of CNP, conventional printing paper, and Bucky paper  
55 and showed that both fiber pull-out and inter-fiber interactions play an important role in CNP  
56 behavior. Meng et al. (Meng et al., 2017) studied the effects of bridging of nanofibrils on the  
57 macroscale fracture toughness of CNP. Miao et al. (Chengyun Miao et al., 2020) comparatively  
58 evaluated crack initiation and growth behaviors of CNP made by two methods namely casting and  
59 filtration, and observed increasing crack growth resistance during the entire fracture process  
60 starting from crack initiation to significant growth. Their results also showed that the CNP made  
61 by the filtration method outperformed the cast counterpart in terms of mechanical properties. All  
62 the reported works on fracture of CNP to date, however, have primarily focused on quasi-static  
63 fracture. The possibility of re-formation of hydrogen bonds as well as observed craze-like features

64 along the crack flanks due to crack growth in this three-dimensionally entangled nanofibrous  
65 material rises the possibility of loading rate dependent fracture behavior. Thus, a comprehensive  
66 fracture performance assessment of CNP, however, should include evaluation of both static and  
67 dynamic fracture characteristics. In fact, it is well-known that fracture of polymer-based  
68 composites with fibrous constituents such as the conventional fiber reinforced polymer composites  
69 (D. Lee et al., 2010; C. Miao & Tippur, 2019) and CNF hydrogel composites (Yang et al., 2019)  
70 are strain rate dependent. Accordingly, the rate dependence of filtered CNP is explored in this  
71 work to bridge this gap.

72 The full-field optical techniques are particularly suitable for investigating fracture  
73 mechanics of CNP. Among the various options available in this regard, Digital Image Correlation  
74 (DIC) technique offers many advantages such as non-contact full-field quantification of  
75 deformations in the region-of-interest (ROI) and simplicity of implementation using recorded  
76 intensities/gray scales to quantify deformations (Chu et al., 1985). Some researchers have applied  
77 DIC to measure thermal expansion of cellulose nanocrystal (CNC) films (Diaz et al., 2013), the  
78 in-plane strain fields on CNP under tension (Zhao et al., 2018), and fracture strength of CNF  
79 hydrogel composite subjected to cyclic loading (Wyss et al., 2018).

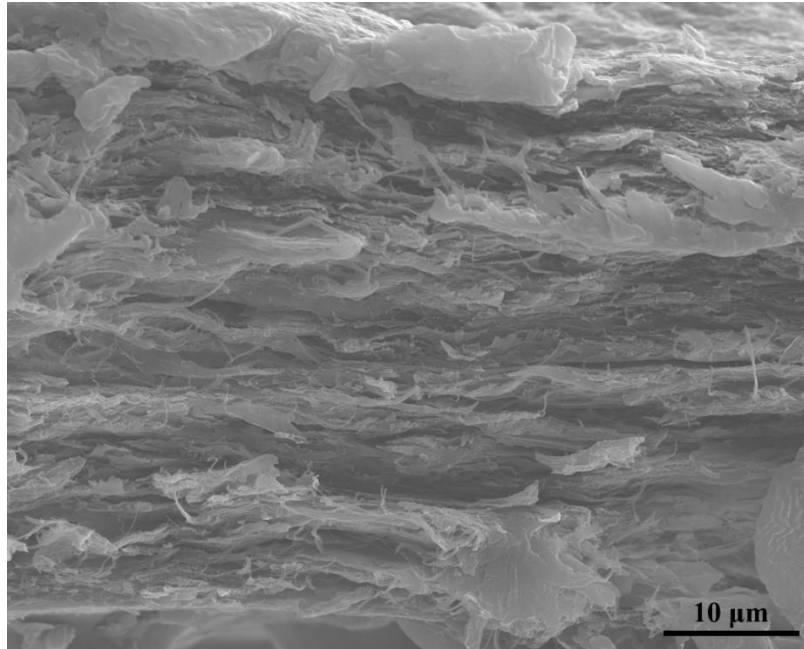
80 This paper is aimed at exploring the dynamic fracture mechanics of CNP. The steps for  
81 preparing CNP is described first. The details about the experiments pertaining to mapping crack  
82 tip fields in single edge notched CNP specimens subjected to dynamic loadings by DIC are  
83 discussed next. This is followed by calculating fracture mechanics parameters (crack velocity,  
84 stress intensity factors and energy release rates) from the DIC measurements. Finally, fracture  
85 mechanics parameters are qualitatively correlated with fractographic features and summarized.

## 86 **2. Experimental Details**

### 87 **2.1 Preparation of CNP**

88 The CNFs aqueous gel at a concentration of around 3 wt.% was obtained from University of Maine,  
89 USA. As noted earlier, the CNP produced for this work was made by a standard *filtration method*  
90 (Parit et al., 2018) and the resulting material was accordingly termed F-CNP. The detailed  
91 procedures for the preparation of the F-CNP can be found in the previous work (Chengyun Miao  
92 et al., 2020). The final F-CNP had a thickness of  $40 \pm 3 \mu\text{m}$ , and density of  $1225 \text{ kg/m}^3$ . As shown

93 in Fig. 1, the morphology of the cross-section of the F-CNP indicates that highly fibrous CNFs  
94 tightly entangled with each other due to strong hydrogen bonding. These abundant hydrogen bonds  
95 could contribute to mechanical strength and fracture characteristics of as-prepared F-CNP. The  
96 Young's modulus was  $10.8 \pm 0.3$  GPa and Poisson's ratio was  $0.23 \pm 0.04$ ; both these elastic  
97 properties were measured separately by performing uniaxial tension tests on F-CNP strips  
98 discussed elsewhere (Chengyun Miao et al., 2020).



99

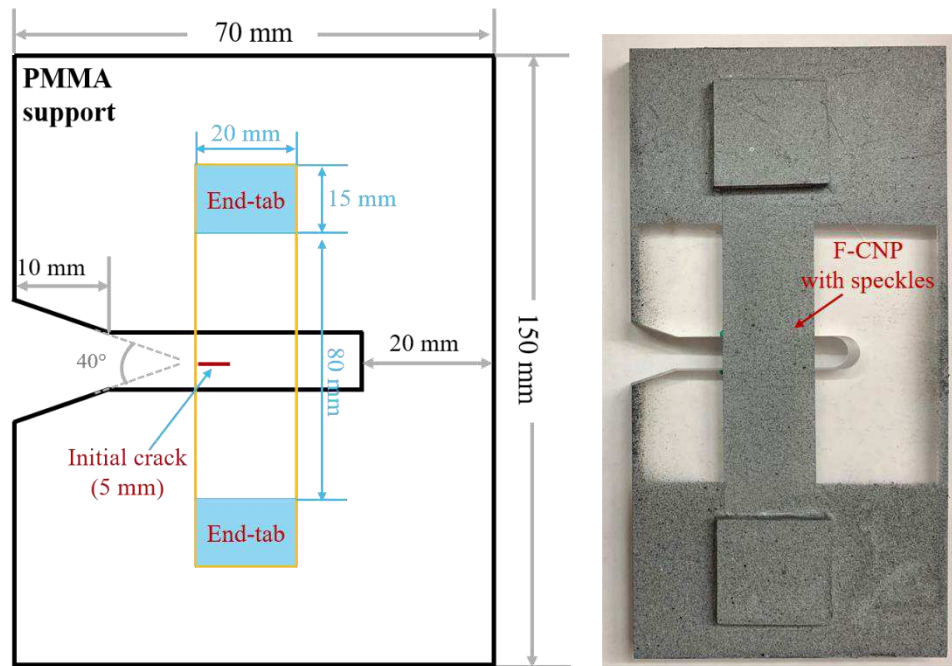
100

Fig.1. SEM image showing the cross-section of F-CNP.

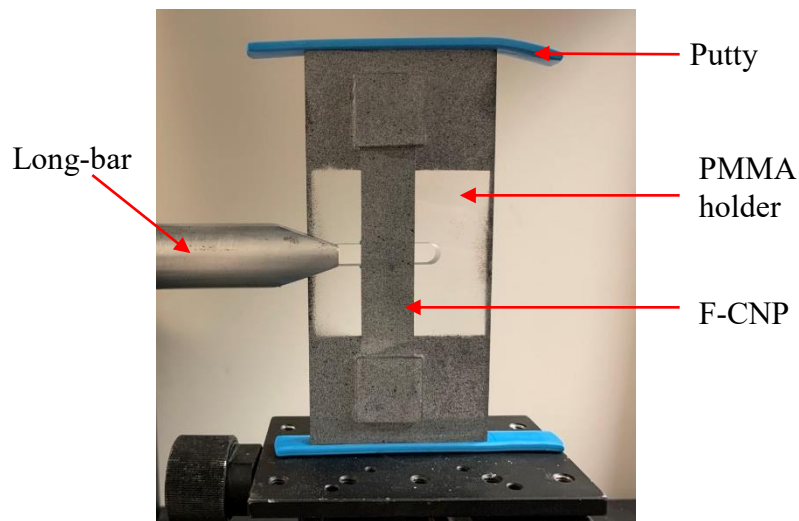
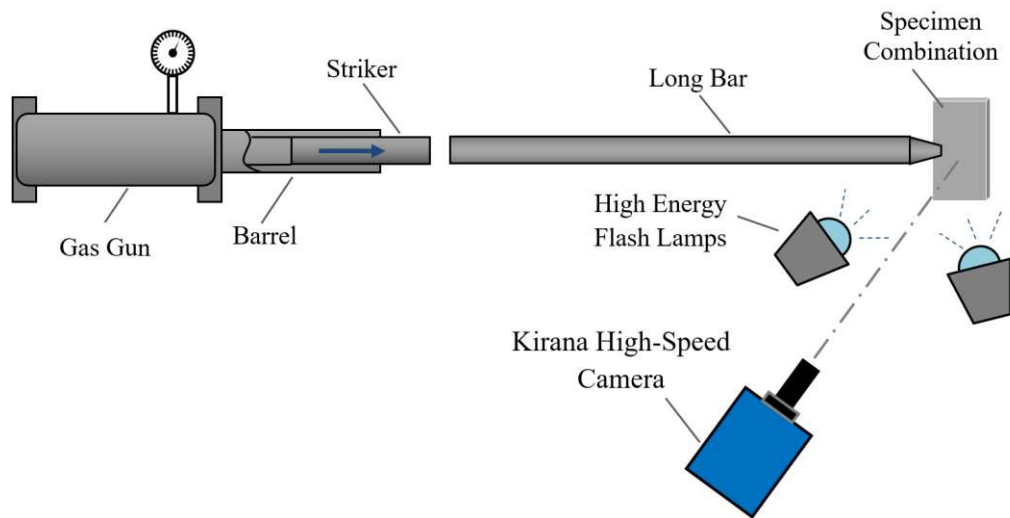
## 101 **2.2. Dynamic Fracture**

102 The dynamic fracture behavior of F-CNP was investigated using DIC along with ultrahigh-speed  
103 photography. Single edge notched (SEN) specimens of dimensions 110 mm × 20 mm were  
104 prepared, and an initial notch of 5 mm length was cut into each of the samples using a sharp razor  
105 blade. To enable high-strain rate loading of F-CNP in mode-I conditions, a special specimen holder  
106 was devised. The holder consisted of a large acrylic (PMMA) support fixture (150 mm × 70 mm  
107 × 8.6 mm), as shown in Fig. 2, to which the specimen was adhered. The acrylic holder had a  
108 symmetric 40° V-notch cut into the middle of the edge of the holder and the V-notch flanks were  
109 extended into the holder as a relatively wide slot (approx. 10 mm wide) with a semicircular tip, as  
110 shown. To this holder, the F-CNP specimen was glued directly. The specimen was sprayed lightly  
111 with random black and white speckles to implement DIC (Chu et al., 1985) and map surface

112 deformations. (The details of the method are intentionally avoided for brevity and can be found in  
113 a number of recent articles and monographs (Kirugulige et al., 2007; Pan et al., 2009; Sutton et al.,  
114 2009; Yoneyama et al., 2006).). The entire F-CNP specimen and the acrylic holder assembly was  
115 subjected to dynamic stress-wave loading along the flanks of the V-notch using a precisely  
116 matching wedge of a modified Hopkinson bar setup. The V-notch and the wide slot in the holder  
117 facilitated rapid tensile loading of the pre-notched F-CNP specimen causing it to fracture well  
118 before the failure of the holder.



119  
120 Fig. 2. Specimen geometry and loading configuration used for dynamic fracture tests: (left)  
121 schematic of specially designed PMMA support; (right) specimen assembly coated with random;  
122 black/white speckles.



123

124 Fig. 3. Schematic (top) and close-up photograph (bottom) of the experimental setup used to study  
 125 dynamic fracture of F-CNP.

126

127

128

129

130

131

132

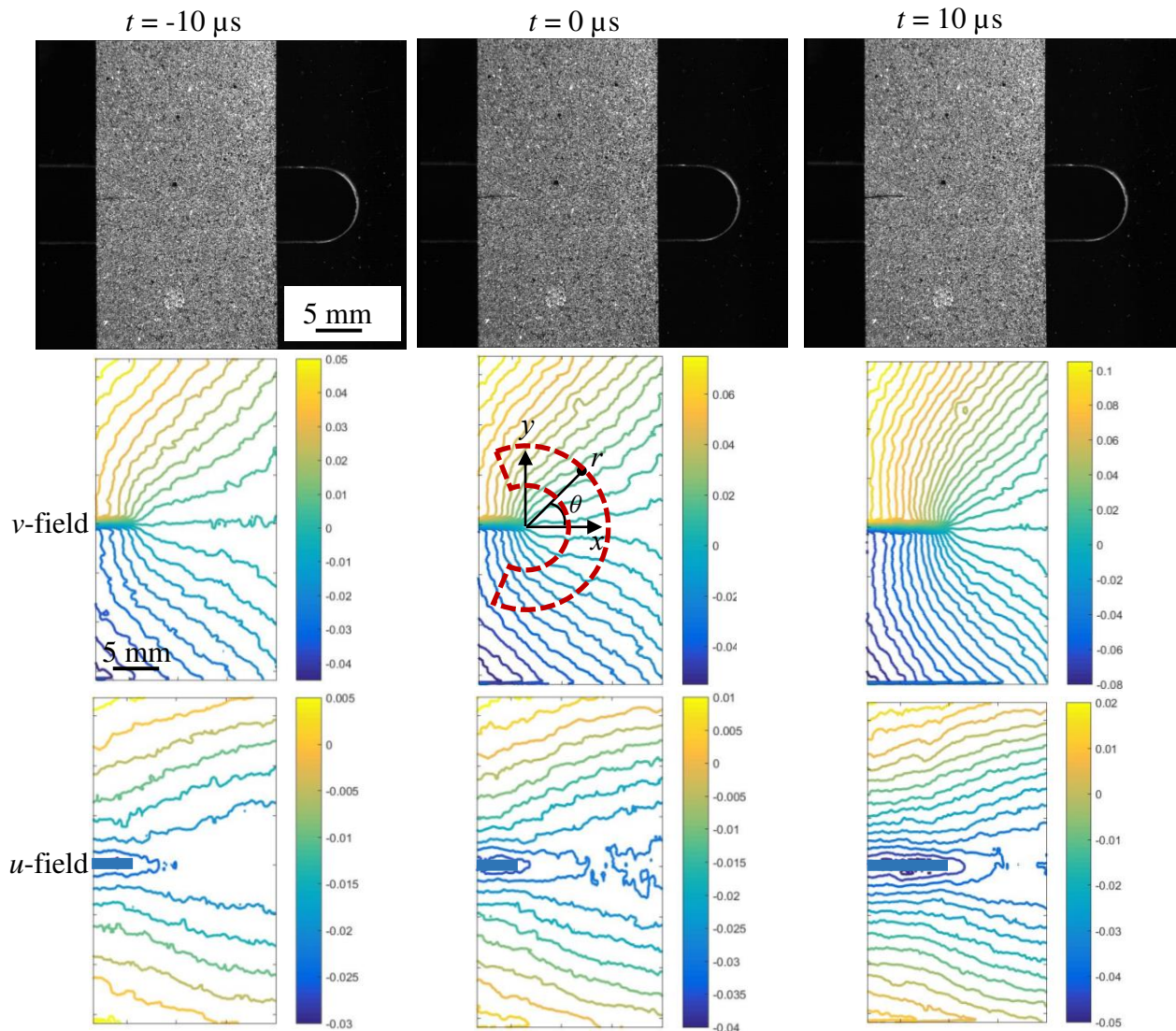
133

The schematic of the experimental setup is shown in Fig. 3. A modified Hopkinson pressure bar was used to impact the acrylic holder to indirectly load the edge notched CNP specimen attached to the holder. The long-bar was 1.83 m long and 25.4 mm in diameter aluminum rod. The tip of the long-bar was machined and polished to be of a wedge-shape to match the V-notch in the acrylic holder. A 305 mm long, 25.4 mm diameter aluminum striker placed in the barrel of a gas-gun was launched towards the long-bar at a velocity of approx. 13 m/s during fracture tests. The compressive stress wave generated by the impact between the striker and the long-bar propagated the length of the long-bar before loading the specimen holder and then the F-

134 CNP specimen. A close-up view of the optical setup is also shown in Fig. 3. Initially, the long-bar  
135 tip was kept in contact with the holder such that the V-notch flanks touched the long-bar. The  
136 specimen holder was placed over a ~1.5 mm thick rectangular soft putty strip on a platform with  
137 another identical putty strip pressed onto the top edge of the holder to achieve symmetry in terms  
138 of the acoustic impedance relative to the loading axis. The speckle images of the specimen  
139 illuminated by a pair of high energy flash lamps were recorded by a Kirana-05M ultrahigh-speed  
140 digital camera at 500,000 frames per second (inter frame period 2  $\mu$ s). When the striker impacted  
141 the long-bar, a trigger pulse was generated to start the recording of the speckle images by the  
142 camera with an adjustable/preset delay. The speckle images were subsequently analyzed using  
143 ARAMIS<sup>®</sup> image analysis software to extract in-plane displacement components,  $u(x, y)$  and  $v(x,$   
144  $y)$  in the  $x$ - and  $y$ -directions, respectively. During analysis, the speckle images were segmented  
145 into facets of size of  $30 \times 30$  pixels (1 pixel = ~44  $\mu$ m on the specimen plane) with 25 pixels  
146 overlap which resulted in approx.  $20 \times 35$  mm<sup>2</sup> region-of-interest (ROI).

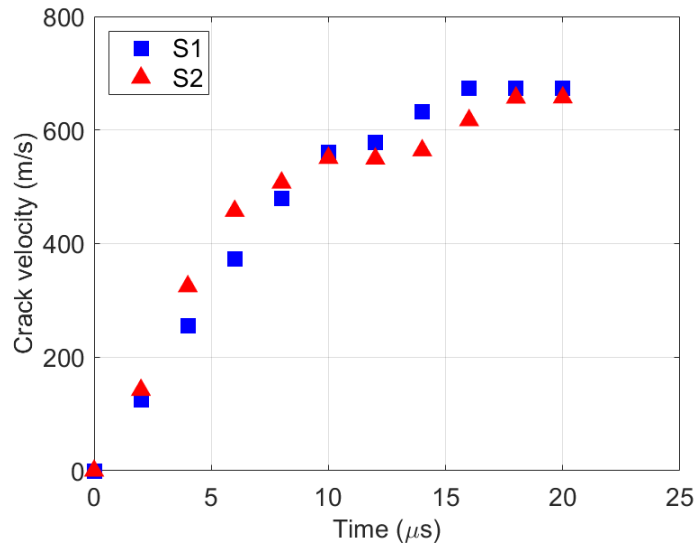
147 The time-resolved speckle images along with the corresponding crack-opening  
148 displacements around a dynamically loaded mode-I crack in the F-CNP specimen are shown in  
149 Fig. 4 at a few select time instants (please see “Supplementary materials” for video). In these plots,  
150  $t = 0$   $\mu$ s corresponds to one frame just before crack initiation at the original crack-tip, and color  
151 bars represent displacements in millimeters. It can be observed that, due to the symmetric nature  
152 of mode-I fracture, the crack propagated self-similarly along a horizontal path (from left to right  
153 in these images) and hence the contours of the two orthogonal displacements are highly symmetric  
154 in shape in case of the  $u$ -field and magnitude in case of the  $v$ -field relative to the initial crack.

155 The crack tip position from crack-opening displacement contours were identified from each  
156 of the images. Subsequently, the crack velocity histories for F-CNP samples were obtained via the  
157 finite difference scheme and are shown in Fig. 5 for two separate tests. It can be observed that the  
158 velocity histories essentially overlap on each other, indicating rather good repeatability of these  
159 experimental results. The crack velocities increase from 0 to ~550 m/s in ~10  $\mu$ s after crack  
160 initiation and then become relatively steady at ~660 m/s, which is equal to ~35%  $C_R$  (Rayleigh  
161 wave speed based on the measured elastic modulus, Poisson’s ratio and mass density).



162

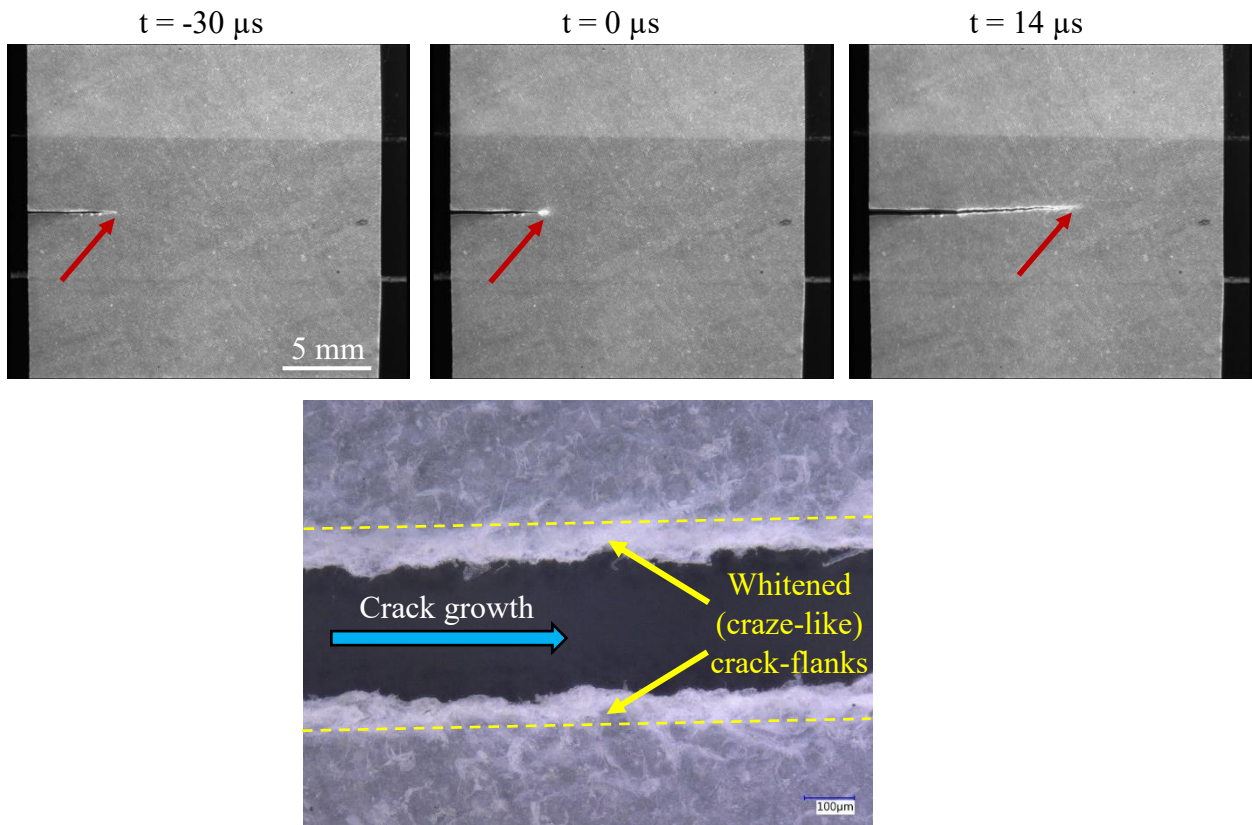
163 Fig. 4. Speckle images (top row) with corresponding measured crack-opening displacement  
 164 contours (middle row) and crack-sliding displacement contours (bottom row) for dynamic fracture  
 165 of F-CNP. Contours are shown in 10  $\mu\text{m}$  increments and the color bar scale is in mm. See  
 166 “Supplementary materials”.



167

168

Fig. 5. Measured crack velocities for two dynamically loaded F-CNP specimens.



169

170 Fig. 6. (Top-row) Images of dynamic crack tip (denoted by the red arrow) propagation in F-CNP  
 171 sample showing whitened zone. (Bottom) Micrograph of fractured specimen edges showing  
 172 whitened crack flanks (blue arrow indicates the crack growth direction). See "Supplementary  
 173 materials".

174 The surface features of F-CNP were examined during fracture in real-time with the aid of  
175 ultrahigh-speed photography on a third specimen without decorating it speckles. That is, the  
176 dynamic fracture on a F-CNP sample without speckles was repeated by focusing the camera on  
177 the surface directly to see details near the crack tip vicinity during dynamic crack propagation.  
178 Three selected real-time images are shown in the top row of Fig. 6 (please see “Supplementary  
179 materials” for video). In these images,  $t = -30 \mu s$  corresponds to the state before the specimen  
180 experiences dynamic loading, hence, no deformation at the original crack tip can be discerned. The  
181  $t = 0 \mu s$  image corresponds to the time instant one frame before crack initiation at the original  
182 crack tip. In this image, a whitened zone ahead and around the crack tip can be clearly observed.  
183 During crack propagation, the whitened zone also appears along the two crack flanks seen at the  
184 time instant  $t = 14 \mu s$ . It can be also found that the whitened zone at  $t = 0 \mu s$  appears wider than  
185 that the one at  $t = 14 \mu s$ , attributable to the development of an inelastic deformation zone within  
186 which CNF are pulled apart prior to crack initiation. The whitened zone ahead of the crack tip  
187 during the crack propagation is relatively long and narrow, potentially due to the combined effects  
188 of bridged fibers behind the crack tip and stretched fibers ahead of crack tip. These could contribute  
189 to the enhancement of crack growth resistance. The edges of this fractured specimen were observed  
190 using a Keyence VHX-6000 series digital microscope, and a representative image is shown in  
191 bottom row of Fig. 6. It is evident that the whitened zone appears along the crack path. This craze-  
192 like appearance, similar to the one often seen in many engineering polymers, could contribute to  
193 resistance of the material to crack growth through inelastic deformations. A similar phenomenon  
194 is also observed during fracture of CNF reinforced hydrogels (Yang et al., 2019).

### 195 **3. Extraction of stress intensity factors (SIFs)**

196 The stress intensity factor (SIF) histories were calculated using an over-deterministic least-  
197 squares analysis of crack-opening displacement contours,  $v(x, y)$ , measured by DIC. The  
198 asymptotic expression for the  $v$ -field around the dynamically propagating crack-tip can be  
199 expressed as (Jajam et al., 2013; Nishioka & Atluri, 1983):

$$\begin{aligned}
v(r, \theta) = & \sum_{n=1}^N \frac{(K_I)_n B_I(V)}{2\mu} \sqrt{\frac{2}{\pi}} (n+1) \left\{ -\beta_1 r_1^{\frac{n}{2}} \sin \frac{n}{2} \theta_1 + \frac{h(n)}{\beta_2} r_2^{\frac{n}{2}} \sin \frac{n}{2} \theta_2 \right\} \\
& + \sum_{n=1}^N \frac{(K_{II})_n B_{II}(V)}{2\mu} \sqrt{\frac{2}{\pi}} (n+1) \left\{ \beta_1 r_1^{\frac{n}{2}} \cos \frac{n}{2} \theta_1 + \frac{h(\bar{n})}{\beta_2} r_2^{\frac{n}{2}} \cos \frac{n}{2} \theta_2 \right\}
\end{aligned} \tag{1}$$

200 where  $v$  is the crack-opening displacement,  $(r, \theta)$  denotes the crack-tip polar coordinates as shown  
201 in Fig. 4. The discrete  $v$ -field data in the region around the crack-tip,  $3 \text{ mm} \leq r \leq 6 \text{ mm}$ ,  $-120^\circ \leq$   
202  $\theta \leq 120^\circ$ , was used in the analysis to minimize the uncertainty associated with the precise crack-  
203 tip location yet sufficiently close to the crack-tip. In Eq. (1),  $(K_I)_1 = K_I$  and  $(K_{II})_1 = K_{II}$  denote  
204 the mode-I and mode-II SIFs, respectively,  $r_m = \sqrt{x^2 + \beta_m^2 y^2}$ ,  $\theta_m = \tan^{-1} \left( \frac{\beta_m y}{x} \right)$ ,  $m = 1, 2$ ,  
205  $\beta_1 = \sqrt{1 - \left( \frac{V}{C_I} \right)^2}$ ,  $\beta_2 = \sqrt{1 - \left( \frac{V}{C_S} \right)^2}$ ,  $C_I = \sqrt{\frac{(\kappa+1)\mu}{(\kappa-1)\rho}}$ ,  $C_S = \sqrt{\frac{\mu}{\rho}}$ ,  $\kappa = \frac{3-\nu}{1+\nu}$  for plane stress,  $V, \mu, \rho$ ,  
206  $\nu$  are the crack velocity, shear modulus, mass density and Poisson's ratio of F-CNP, respectively.  
207 The remaining functions in Eq. (1) are defined as,

$$208 \quad h(n) = \frac{2\beta_1\beta_2}{1+\beta_2} \text{ for } n=\text{odd}, \quad h(n) = \frac{1+\beta_2^2}{2} \text{ for } n=\text{even} \quad \text{and} \quad h(\bar{n}) = h(n+1);$$

$$209 \quad B_I(V) = \frac{1+\beta_2^2}{D}, \quad B_{II}(V) = \frac{2\beta_2}{D}, \quad D = 4\beta_1\beta_2 - (1+\beta_2^2)^2.$$

210 In the above equation, the effect of non-singular far-field deformations, if any, on the measured  $K_I$   
211 and  $K_{II}$  was offset by using four higher order terms ( $N=4$ ) while performing least-squares analysis.  
212 It should also be noted that the crack-tip displacements were forced to be zero during the analysis.

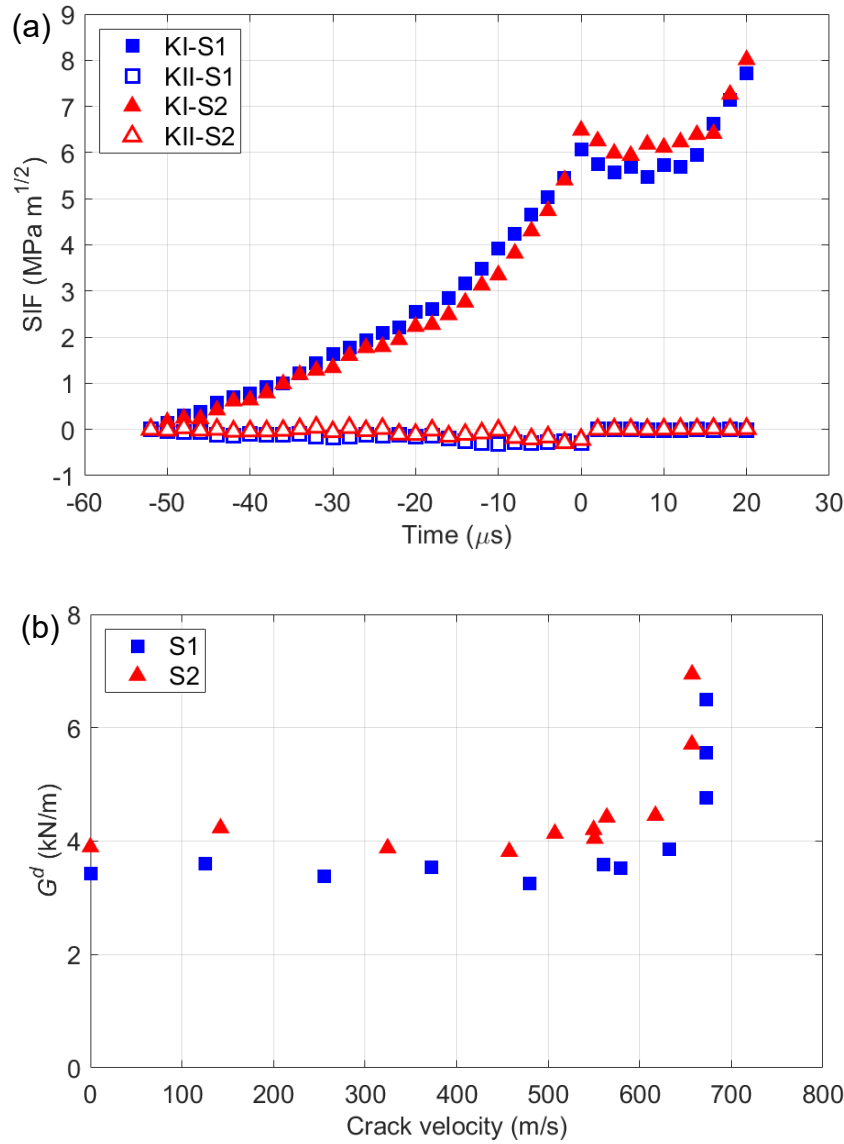
213 The measured crack velocities,  $V$  and SIFs were used to calculate the dynamic energy  
214 release rates for dynamically growing cracks using (K. Ravi-Chandar, 2004):

$$G^d = \frac{1}{E} [A_I(V)K_I^2 + A_{II}(V)K_{II}^2] \tag{2}$$

$$215 \quad \text{where } A_I(V) = \frac{V^2\beta_1}{(1-\nu)C_S^2 D}, \quad A_{II}(V) = \frac{V^2\beta_2}{(1-\nu)C_S^2 D}.$$

## 216 4. Results and discussion

217 **4.1 Dynamic fracture**



218

219

220 Fig. 7. Dynamic fracture parameters for two F-CNP specimens: (a) Measured stress intensity factor  
 221 (SIF) histories,  $t = 0$  corresponds to crack initiation; (b) Variation of dynamic strain energy release  
 222 rates with crack velocity.

223 The dynamic SIFs calculated from Eq. (1) are plotted for two specimens in Fig. 7(a). The time axis  
 224 of these plots was shifted so that  $t = 0$  corresponds to crack initiation at the original edge crack-  
 225 tip. The solid and open symbols represent SIFs,  $K_I$  and  $K_{II}$ , respectively. The  $K_I$  histories increase  
 226 monotonically for both specimens, almost linearly in the beginning, until crack initiation. The  
 227 dynamic fracture toughness ( $K_I$  at  $t = 0$ ) was recorded at  $6.3 \pm 0.3 \text{ MPa m}^{1/2}$ . The time rate of

228 change of  $K_I$ , or  $\frac{dK_I}{dt}$ , was  $\sim(4.3 \pm 1.6) \times 10^5$  MPa m<sup>1/2</sup>/s at crack initiation based on a few data points  
229 in the  $K_I$  history just prior to initiation. It can be observed that there is a drop in the  $K_I$  histories  
230 immediately after crack initiation to  $\sim 5.6$  MPa m<sup>1/2</sup>, which is due to dynamic unloading following  
231 crack initiation from the stationary tip. Subsequently, the  $K_I$  histories increase monotonically again  
232 until the end of the observation window, consistent with the craze-like phenomenon that occurred  
233 during crack propagation, shown in Fig. 6. The fibrous and tortuous crack path effectively  
234 increases the resistance to crack growth. The  $K_{II}$  histories throughout the observation window are  
235 nearly zero, in both the pre- and post-crack initiation regimes, due to nominally mode-I fracture.  
236 The nonzero values of  $K_{II}$  suggest potential error in the least-squares analysis and locating of the  
237 crack tip during data analysis. The two sets of experimental results essentially agree with each  
238 other indicating very good reproducibility of these experiments.

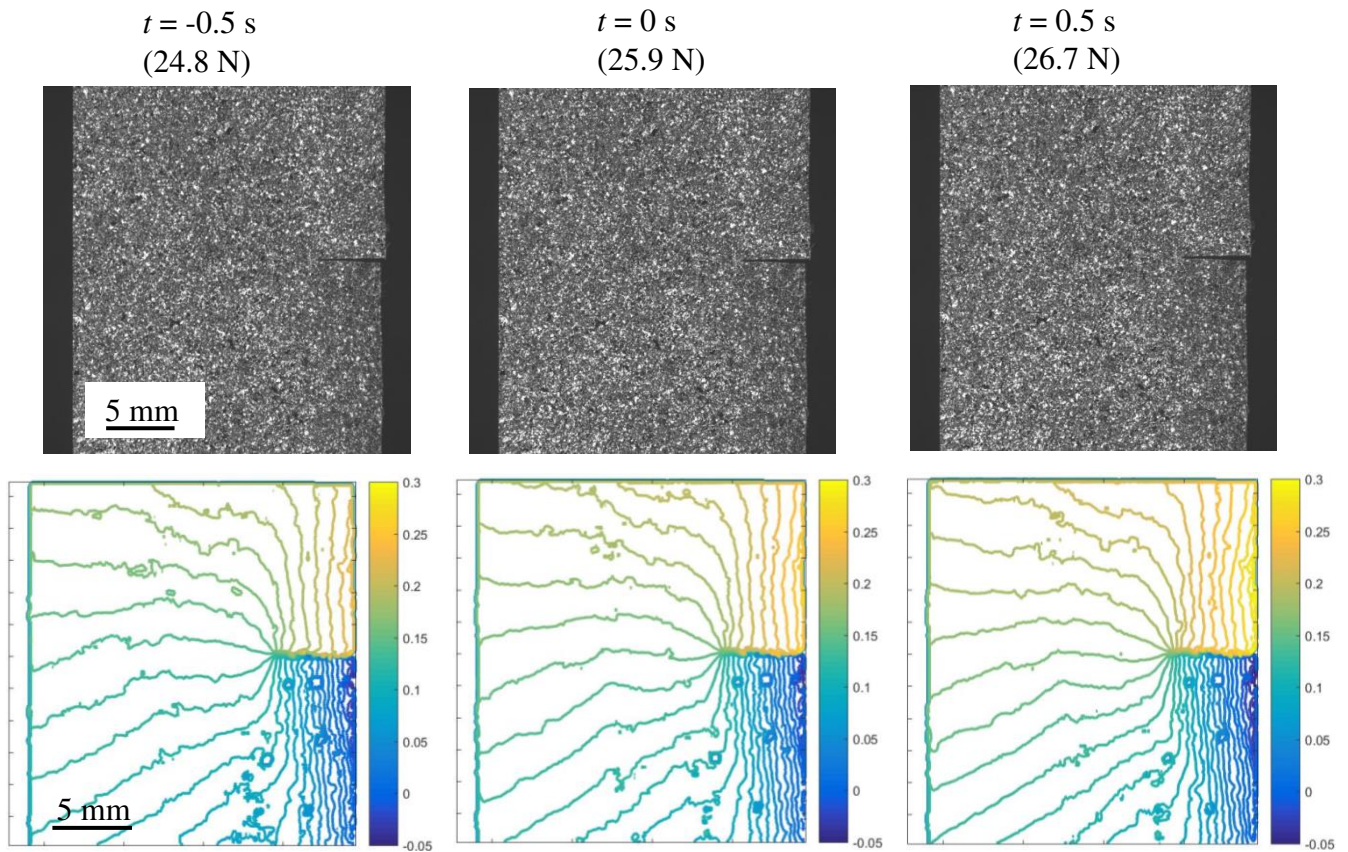
239 The dynamic SIFs are a function of crack velocity and loading rate ( $\frac{dK_I}{dt}$ ) (K. Ravi-Chandar,  
240 2004). Accordingly, using measured crack velocities  $V$  in Fig. 5 and post-initiation stress intensity  
241 factors  $K_I$  and  $K_{II}$  in Fig. 7(a), the dynamic energy release rates ( $G^d$ ) for growing cracks were  
242 evaluated from Eq. (2). The results are plotted in Fig. 7(b). It can be observed that the  
243 measured value of  $G^d$  is  $\sim 3.7$  kN/m at crack initiation. After crack initiation,  $G^d(V)$  is nearly a  
244 constant initially, ranging between  $\sim 3.4$  to  $\sim 4.4$  kN/m, until crack velocity reaches  $\sim 620$  m/s.  
245 Later on, the  $G^d$  values dramatically increase (to  $\sim 7$  kN/m within the observation window) in what  
246 appears to be a narrow terminal velocity range of 620-670 m/s for this material.

## 247 **4.2 Comparison with quasi-static fracture behavior**

248 The quasi-static fracture of F-CNP single edge-notched (SEN) specimens subjected to uniaxial  
249 tension was investigated by the authors in a previous study (Chengyun Miao et al., 2020). Those  
250 results are compared with the dynamic counterparts to infer the loading rate effects. The  
251 experimental details are intentionally not included here for the sake of brevity and the readers can  
252 find those details in Ref. (Chengyun Miao et al., 2020).

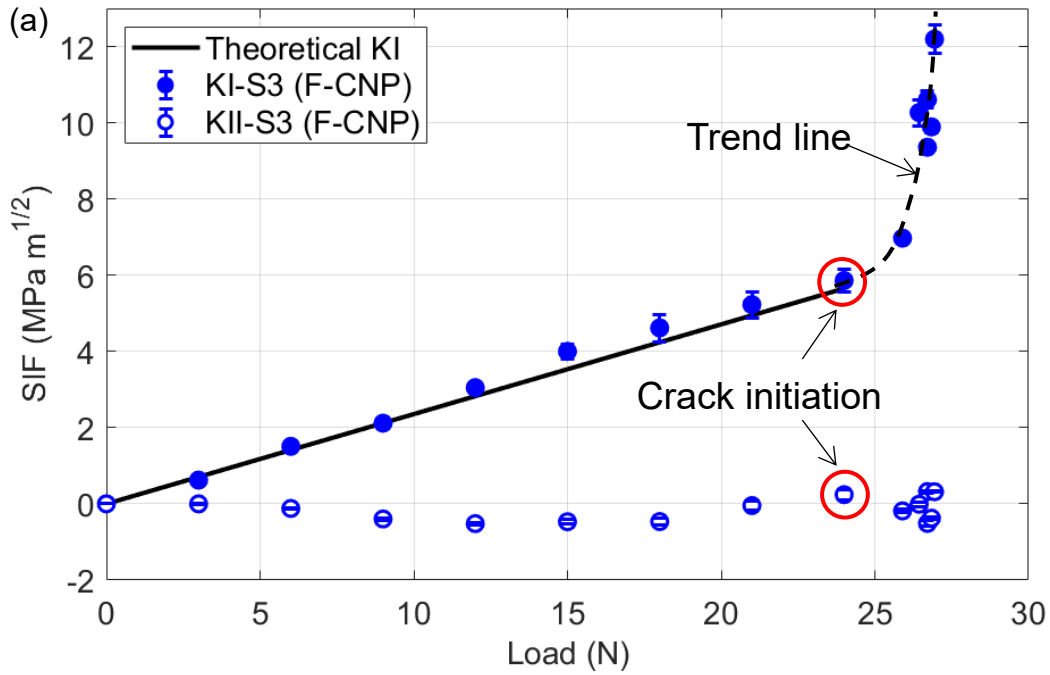
253 The speckle images and the related crack-opening displacement contours ( $v$ -field) for a few  
254 select time instants are shown in Fig. 8. In these plots,  $t = 0$  s corresponds to the recorded image  
255 just before crack initiation. The specimen here was also subjected to mode-I loading conditions  
256 and hence contours in  $v$ -field displacements are nominally symmetric in shape and magnitude

257 relative to the crack. However, when compared to the  $v$ -field contours for the dynamic fracture  
 258 cases shown in Fig. 4, there is more noise in these contours due to the rigid body motions that are  
 259 essentially negligible during dynamic fracture event due to the short observation window of approx.  
 260 80 microseconds. Furthermore, the displacement contours behind the crack-tip show asymmetry;  
 261 that is, more contours on the lower half of the specimen relative to the upper half. Tests on other  
 262 specimens have also produced similar results despite exercising care to eliminate misalignment.  
 263 This suggests a failure mechanism unique to F-CNP that produces an out-of-plane deflection of  
 264 crack flanks due to fiber entanglement. This in turn causes antisymmetric but pseudo crack opening  
 265 displacements in addition to the actual mode-I deformations. The crack opening displacement  
 266 contours ahead of the crack, however, remain unaffected and follow expected trends of a mode-I  
 267 crack and hence can be analyzed (C. Miao et al., 2020).

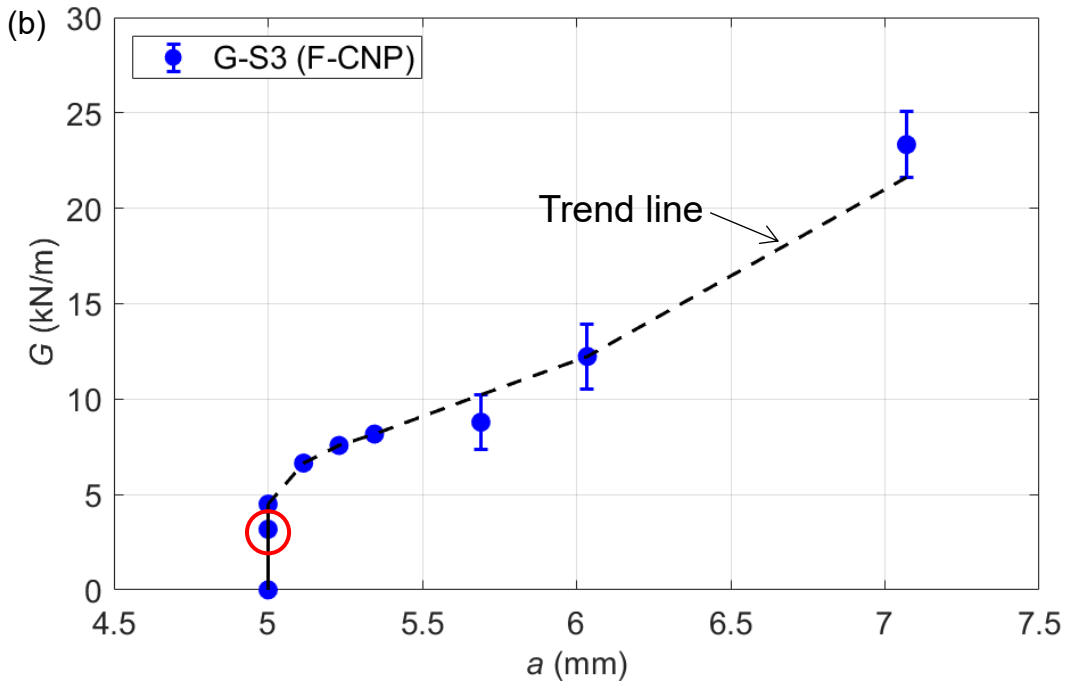


268  
 269 Fig. 8. Speckle images (top row) with corresponding measured crack-opening displacement  
 270 contours (bottom row) for quasi-static fracture of F-CNP. Contours are shown in 10  $\mu$ m increments  
 271 and the color bar scale is in mm.

272



273



274

275 Fig. 9. Fracture parameters for F-CNP subjected to quasi-static fracture: (a) Measured stress  
 276 intensity factor (SIF) histories at different loads levels; (b) Strain energy release rates in the post-  
 277 crack initiation regime. Solid line indicates values before crack initiation, dotted line indicates  
 278 unstable crack growth.

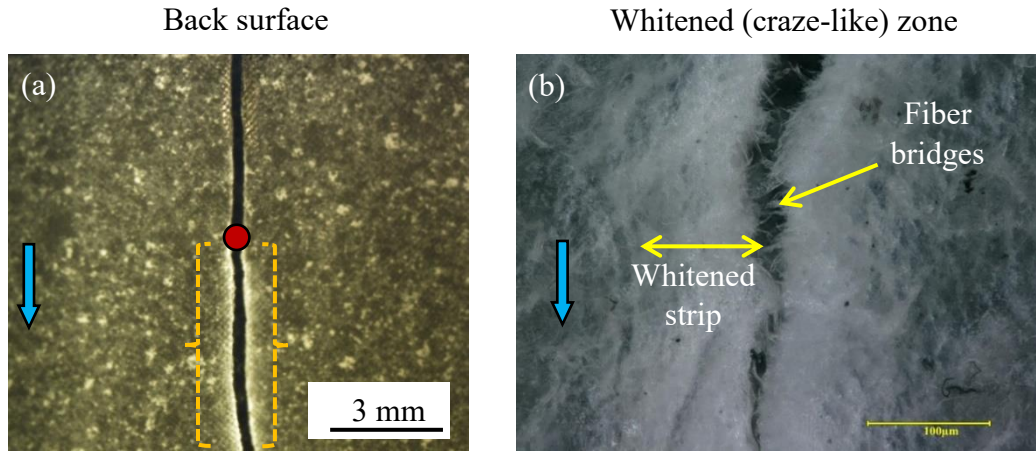
279

280 The measured  $\nu$ -field results from DIC for one representative specimen (#S3) subjected to  
281 quasi-static loading were used to calculate the SIFs in both the pre- and post-crack initiation  
282 regimes. The mode-I SIFs in the pre-crack initiation regime were comparatively examined relative  
283 to the theoretical counterparts based on the measured load history at 3 N intervals until crack  
284 initiation. The comparison between these two is shown in Fig. 9(a). The solid and open symbols  
285 represent  $K_I$  and  $K_{II}$ , respectively. The solid line corresponds to the theoretical values. It can be  
286 observed from the plot that the quasi-static fracture toughness for F-CNP is  $\sim 5.9 \text{ MPa m}^{1/2}$ . The  
287 loading rate assessed in terms of time rate of change of  $K_I$ , or  $\frac{dK_I}{dt}$ , is  $\sim (6 \pm 0.5) \times 10^{-1} \text{ MPa m}^{1/2}/\text{s}$  at  
288 crack initiation based on a few data points in the  $K_I$  history leading up to initiation. It is evident in  
289 Fig. 9(a) that there is a good agreement between the experimental and theoretical values of mode-  
290 I SIF from linear elastic fracture mechanics. It should be noted here that the fracture toughness  
291 value of F-CNP is at least 50% higher than that for polycarbonate (PC), a tough engineering  
292 polymer known for its superior ductility and fracture toughness. The mode-I SIFs in the post-crack  
293 initiation regime are also plotted in Fig. 9(a) and they increase dramatically, up to  $12 \text{ MPa m}^{1/2}$ ,  
294 suggesting that F-CNP, a natural biopolymer, is capable of offering highly desirable crack growth  
295 resistance during crack growth. The mode-II SIF values are also plotted for completeness even  
296 though the loading was nominally mode-I. The non-zero and negligibly small values of  $K_{II}$  help  
297 provide error estimates due to least-squares analysis approach of extracting SIFs.

298 To quantify the crack growth resistance characteristic of F-CNP noted above, the strain  
299 energy release rate ( $G$ ) was evaluated using the SIFs in the post-crack initiation regime. Knowing  
300 the crack length at each load level, plots of  $G$  vs.  $a$  (crack length), or the so-called crack growth  
301 resistance curve, was obtained and is shown in Fig. 9(b). It can be observed that values of  $G$  for F-  
302 CNP increase from  $\sim 3.2 \text{ kN/m}$  at initiation to  $\sim 23.3 \text{ kN/m}$  towards the end of the observation  
303 window. Again, this increasing trend of  $G$  displays a desirable resistance to crack growth of F-  
304 CNP.

305 The fractography of F-CNP subjected to quasi-static fracture performed using an optical  
306 microscope and is shown in Fig. 10(a). A narrow strip of whitened region relative to the  
307 surroundings, marked by yellow braces in the figure, was observed along the two crack flanks on  
308 the specimens. These fractured edges were also observed using Keyence VHX-6000 series digital  
309 microscope and is shown in Fig. 10(b). A highly tortuous crack path among the entangled fibers

310 in the whitened region suggest fracture toughening. The similar whitened zone was also observed  
 311 in the dynamic fracture counterpart shown in Fig. 6. However, it should be noted here that  
 312 fractography in the quasi-static counterpart revealed the occurrence of the whitened zone only in  
 313 the wake of the crack.



314  
 315 Fig. 10. Quasi-static crack growth features for F-CNP: (a) Image of back surface of F-CNP. (b)  
 316 Micrographs of fractured specimen edges close to the crack tip. The blue arrow indicates the crack  
 317 growth direction, and the red dot is the initial notch tip.

### 318 5. Concluding Remarks

319 Dynamic fracture behaviors of filtered cellulose nanopaper (F-CNP) are experimentally studied in  
 320 this work by subjecting single-edge notched specimens to symmetric tensile loading. The dynamic  
 321 loading of F-CNP is achieved by a specially devised acrylic holder with a wide pre-cut slot bridged  
 322 by a CNP strip with an edge crack. The 2D-DIC methodology is used to measure deformations in  
 323 the crack vicinity quantitatively by recording images in both the pre- and post-crack initiation  
 324 regimes via ultrahigh-speed photography. The crack opening displacements measured from DIC  
 325 are used to calculate the fracture parameters in the entire fracture process. The results of quasi-  
 326 static fracture behavior of F-CNP are also included here to comparatively show the loading rate  
 327 effects.

328 The measured fracture toughness of  $\sim 6.3 \text{ MPa m}^{1/2}$  under dynamic loading conditions ( $\frac{dK_I}{dt}$ )  
 329  $\sim 4.3 \times 10^5 \text{ MPa m}^{1/2}/\text{s}$ ) is slightly higher than  $\sim 5.9 \text{ MPa m}^{1/2}$  from quasi-static ( $\frac{dK_I}{dt}$ )  $\sim 6 \times 10^{-1} \text{ MPa}$   
 330  $\text{m}^{1/2}/\text{s}$ ) experiments. It should be noted that this increase for a low density ( $1225 \text{ kg/m}^3$ ) fibrous  
 331 biodegradable natural material with a relatively high elastic modulus (10 GPa) is unlike those

332 evident in conventional composites. (That is, the behavior is contrary to fiber reinforced  
333 composites which often show lower fracture toughness under dynamic loading conditions relative  
334 to the quasi-static counterparts (C. Miao & Tippur, 2019) in matrix dominant orientations.)  
335 Furthermore, the crack initiation toughness of F-CNP is significantly higher than tough  
336 engineering polymers such as polycarbonate, for which the reported fracture toughness is in the  
337 range 3-4 MPa m<sup>1/2</sup> with a significantly lower elastic modulus of ~2.5 GPa under quasi-static  
338 conditions and ~2.0 MPa m<sup>1/2</sup> under dynamic conditions (Sundaram & Tippur, 2017). These  
339 suggest a clear superiority of F-CNP in terms of fracture behavior under both quasi-static and  
340 dynamic loading conditions.

341 In the post-crack initiation regime, the increase of strain energy release rate is approximately  
342 seven-fold, starting from ~3.2 to ~23.3 kN/m, in the observation window under quasi-static  
343 conditions. Under dynamic conditions, the energy release rates also show a rapid increase from  
344 ~3.4 to >7 kN/m as the crack speed reaches terminal speed in the 620-670 m/s range. Thus, F-  
345 CNP shows increasing crack growth resistance in both quasi-static and dynamic loading conditions  
346 and at two vastly different loading rates, indicating superior fracture behavior during crack growth.  
347 The postmortem examination and fractography of crack flanks suggest that the crack growth  
348 resistance is primarily due to the formation of whitened strips evident all along the crack path. The  
349 synergistic effects of bridged fibers across the crack faces, microscale tortuosity in the crack path  
350 and fiber pull-outs ahead of the crack tip increase the resistance of F-CNP to crack growth. It is  
351 well-known that under dynamic conditions, material ductility in case of polymers (Sundaram &  
352 Tippur, 2017) and microcracking ahead of crack tip in case of brittle materials (Chengyun Miao  
353 & V Tippur, 2020), are common sources of crack growth resistance. Thus, the observed  
354 toughening in F-CNP is in some ways different from these well-known situations, which indicates  
355 the uniqueness of crack growth characteristics in F-CNP.

### 356 **Acknowledgement**

357 Haishun Du acknowledges the financial support from the China Scholarship Council (No.  
358 201708120052).

### 359 **Appendix**

360 The following are the Supplementary materials to this article:

361 Video of dynamic crack propagation for  $v$ -field; Video of dynamic crack propagation for  $u$ -field;  
362 Video of dynamic crack propagation in F-CNP showing whitened zone.

363 **Compliance with ethical standards**

364 **Conflict of interest**

365 There is no conflict of interest.

366 **Ethical approval**

367 This article does not contain any studies with human participants or  
368 animals performed by any of the authors.

369 **References:**

370 Benítez, A. J., & Walther, A. (2017). Cellulose nanofibril nanopapers and bioinspired  
371 nanocomposites: A review to understand the mechanical property space. *Journal of*  
372 *Materials Chemistry A*, 5(31), 16003–16024. <https://doi.org/10.1039/c7ta02006f>

373 Chen, Y., Zhang, L., Mei, C., Li, Y., Duan, G., Agarwal, S., Greiner, A., Ma, C., & Jiang, S.  
374 (2020). Wood-Inspired Anisotropic Cellulose Nanofibril Composite Sponges for  
375 Multifunctional Applications. *ACS Applied Materials & Interfaces*.  
376 <https://doi.org/10.1021/acsami.0c10645>

377 Chu, T. C., Ranson, W. F., & Sutton, M. A. (1985). Applications of digital-image-correlation  
378 techniques to experimental mechanics. *Experimental Mechanics*, 25(3), 232–244.  
379 <https://doi.org/10.1007/BF02325092>

380 Diaz, J. A., Wu, X., Martini, A., Youngblood, J. P., & Moon, R. J. (2013). Thermal expansion of  
381 self-organized and shear-oriented cellulose nanocrystal films. *Biomacromolecules*, 14(8),  
382 2900–2908. <https://doi.org/10.1021/bm400794e>

383 Du, H., Liu, W., Zhang, M., Si, C., Zhang, X., & Li, B. (2019). Cellulose nanocrystals and  
384 cellulose nanofibrils based hydrogels for biomedical applications. *Carbohydrate Polymers*,  
385 209, 130–144. <https://doi.org/10.1016/J.CARBPOL.2019.01.020>

386 Du, H., Parit, M., Wu, M., Che, X., Wang, Y., Zhang, M., Wang, R., Zhang, X., Jiang, Z., & Li,

387 B. (2020). Sustainable valorization of paper mill sludge into cellulose nanofibrils and  
388 cellulose nanopaper. *Journal of Hazardous Materials*, 400(May), 123106.  
389 <https://doi.org/10.1016/j.jhazmat.2020.123106>

390 Jajam, K. C., Bird, S. A., Auad, M. L., & Tippur, H. V. (2013). Tensile, fracture and impact  
391 behavior of transparent Interpenetrating Polymer Networks with polyurethane-poly(methyl  
392 methacrylate). *Polymer Testing*, 32(5), 889–900.  
393 <https://doi.org/10.1016/J.POLYMERTESTING.2013.04.010>

394 Jung, Y. H., Chang, T. H., Zhang, H., Yao, C., Zheng, Q., Yang, V. W., Mi, H., Kim, M., Cho,  
395 S. J., Park, D. W., Jiang, H., Lee, J., Qiu, Y., Zhou, W., Cai, Z., Gong, S., & Ma, Z. (2015).  
396 High-performance green flexible electronics based on biodegradable cellulose nanofibril  
397 paper. *Nature Communications*, 6(May). <https://doi.org/10.1038/ncomms8170>

398 Kargarzadeh, H., Huang, J., Lin, N., Ahmad, I., Mariano, M., Dufresne, A., Thomas, S., &  
399 Gałęski, A. (2018). Recent developments in nanocellulose-based biodegradable polymers,  
400 thermoplastic polymers, and porous nanocomposites. *Progress in Polymer Science*, 87,  
401 197–227. <https://doi.org/10.1016/J.PROGPOLYMSCI.2018.07.008>

402 Kirugulige, M. S., Tippur, H. V., & Denney, T. S. (2007). Measurement of transient deformations  
403 using digital image correlation method and high-speed photography: application to dynamic  
404 fracture. *Appl. Opt.*, 46(22), 5083–5096. <https://doi.org/10.1364/AO.46.005083>

405 Lee, D., Tippur, H., & Bogert, P. (2010). Quasi-static and dynamic fracture of graphite/epoxy  
406 composites: An optical study of loading-rate effects. *Composites Part B: Engineering*,  
407 41(6), 462–474. <https://doi.org/10.1016/J.COMPOSITESB.2010.05.007>

408 Lee, K. Y., Aitomäki, Y., Berglund, L. A., Oksman, K., & Bismarck, A. (2014). On the use of  
409 nanocellulose as reinforcement in polymer matrix composites. *Composites Science and  
410 Technology*, 105(December), 15–27. <https://doi.org/10.1016/j.compscitech.2014.08.032>

411 Liu, W., Du, H., Zhang, M., Liu, K., Liu, H., Xie, H., Zhang, X., & Si, C. (2020). Bacterial  
412 Cellulose-Based Composite Scaffolds for Biomedical Applications: A Review. *ACS  
413 Sustainable Chemistry and Engineering*, 8(20), 7536–7562.  
414 <https://doi.org/10.1021/acssuschemeng.0c00125>

415 Mao, R., Goutianos, S., Tu, W., Meng, N., Yang, G., Berglund, L. A., & Peijs, T. (2017).  
416 Comparison of fracture properties of cellulose nanopaper, printing paper and buckypaper.  
417 *Journal of Materials Science*, 52(16), 9508–9519. <https://doi.org/10.1007/s10853-017->  
418 1108-4

419 Meng, Q., Li, B., Li, T., & Feng, X.-Q. (2017). A multiscale crack-bridging model of cellulose  
420 nanopaper. *Journal of the Mechanics and Physics of Solids*, 103, 22–39.  
421 <https://doi.org/10.1016/J.JMPS.2017.03.004>

422 Miao, C., Du, H., Parit, M., Jiang, Z., Tippur, H. V., Zhang, X., Liu, Z., Li, J., & Wang, R.  
423 (2020). Superior crack initiation and growth characteristics of cellulose nanopapers.  
424 *Cellulose*, 27(6). <https://doi.org/10.1007/s10570-020-03015-x>

425 Miao, C., & Tippur, H. V. (2019). Fracture behavior of carbon fiber reinforced polymer  
426 composites: An optical study of loading rate effects. *Engineering Fracture Mechanics*, 207.  
427 <https://doi.org/10.1016/j.engfracmech.2018.12.035>

428 Miao, Chengyun, Du, H., Parit, M., Jiang, Z., Tippur, H. V., Zhang, X., Liu, Z., Li, J., & Wang,  
429 R. (2020). Superior crack initiation and growth characteristics of cellulose nanopapers.  
430 *Cellulose*, 27(6), 3181–3195. <https://doi.org/10.1007/s10570-020-03015-x>

431 Miao, Chengyun, & V Tippur, H. (2020). Dynamic Fracture of Soda-lime Glass Plates Studied  
432 using Two Modified Digital Gradient Sensing Techniques. *Engineering Fracture*  
433 *Mechanics*, 232(January), 107048. <https://doi.org/10.1016/j.engfracmech.2020.107048>

434 Nishioka, T., & Atluri, S. N. (1983). Path-independent integrals, energy release rates, and  
435 general solutions of near-tip fields in mixed-mode dynamic fracture mechanics.  
436 *Engineering Fracture Mechanics*, 18(1), 1–22. <https://doi.org/10.1016/0013->  
437 7944(83)90091-7

438 Nogi, M., Karakawa, M., Komoda, N., Yagyu, H., & Nge, T. T. (2015). Transparent Conductive  
439 Nanofiber Paper for Foldable Solar Cells. *Scientific Reports*, 5, 1–7.  
440 <https://doi.org/10.1038/srep17254>

441 Pan, B., Qian, K., Xie, H., & Asundi, A. (2009). Two-dimensional digital image correlation for  
442 in-plane displacement and strain measurement: a review. *Measurement Science and*

443           *Technology*, 20(6), 062001. <https://doi.org/10.1088/0957-0233/20/6/062001>

444 Parit, M., Aksoy, B., & Jiang, Z. (2018). Towards standardization of laboratory preparation  
445 procedure for uniform cellulose nanopapers. *Cellulose*, 25(5), 2915–2924.  
446 <https://doi.org/10.1007/s10570-018-1759-6>

447 Ravi-Chandar, K. (2004). *Dynamic fracture* (K. B. T.-D. F. Ravi-Chandar (ed.)). Elsevier.  
448 <https://doi.org/https://doi.org/10.1016/B978-008044352-2/50008-9>

449 Sundaram, B. M., & Tippur, H. V. (2017). Dynamic mixed-mode fracture behaviors of PMMA  
450 and polycarbonate. *Engineering Fracture Mechanics*, 176, 186–212.  
451 <https://doi.org/10.1016/J.ENGFRACMECH.2017.02.029>

452 Sutton, M. A., Orteu, J.-J., & Schreier, H. (2009). *Image Correlation for Shape, Motion and*  
453 *Deformation Measurements: Basic Concepts, Theory and Applications* (1st ed.). Springer  
454 Publishing Company, Incorporated.

455 Wang, Q., Du, H., Zhang, F., Zhang, Y., Wu, M., Yu, G., Liu, C., Li, B., & Peng, H. (2018).  
456 Flexible cellulose nanopaper with high wet tensile strength, high toughness and tunable  
457 ultraviolet blocking ability fabricated from tobacco stalk: Via a sustainable method. *Journal*  
458 *of Materials Chemistry A*, 6(27), 13021–13030. <https://doi.org/10.1039/c8ta01986j>

459 Wyss, C. S., Karami, P., Bourban, P.-E., & Pioletti, D. P. (2018). Cyclic loading of a  
460 cellulose/hydrogel composite increases its fracture strength. *Extreme Mechanics Letters*, 24,  
461 66–74. <https://doi.org/10.1016/J.EML.2018.09.002>

462 Xie, H., Du, H., Yang, X., & Si, C. (2018). Recent Strategies in Preparation of Cellulose  
463 Nanocrystals and Cellulose Nanofibrils Derived from Raw Cellulose Materials.  
464 *International Journal of Polymer Science*, 2018. <https://doi.org/10.1155/2018/7923068>

465 Xing, J., Tao, P., Wu, Z., Xing, C., Liao, X., & Nie, S. (2019). Nanocellulose-graphene  
466 composites: A promising nanomaterial for flexible supercapacitors. *Carbohydrate*  
467 *Polymers*, 207, 447–459. <https://doi.org/10.1016/j.carbpol.2018.12.010>

468 Yang, J., Shao, C., & Meng, L. (2019). Strain Rate-Dependent Viscoelasticity and Fracture  
469 Mechanics of Cellulose Nanofibril Composite Hydrogels. *Langmuir*, 35(32), 10542–10550.  
470 <https://doi.org/10.1021/acs.langmuir.9b01532>

471 Yoneyama, S., Morimoto, Y., & Takashi, M. (2006). Automatic evaluation of mixed-mode stress  
472 intensity factors utilizing digital image correlation. *Strain*, 42(1), 21–29.  
473 <https://doi.org/10.1111/j.1475-1305.2006.00246.x>

474 Zhao, M., Ansari, F., Takeuchi, M., Shimizu, M., Saito, T., Berglund, L. A., & Isogai, A. (2018).  
475 Nematic structuring of transparent and multifunctional nanocellulose papers. *Nanoscale*  
476 *Horizons*, 3(1), 28–34. <https://doi.org/10.1039/c7nh00104e>

477 Zhu, H., Zhu, S., Jia, Z., Parvinian, S., Li, Y., Vaaland, O., Hu, L., & Li, T. (2015). Anomalous  
478 scaling law of strength and toughness of cellulose nanopaper. *Proceedings of the National*  
479 *Academy of Sciences*, 112(29), 8971–8976. <https://doi.org/10.1073/PNAS.1502870112>

480

## Supplementary Files

This is a list of supplementary files associated with this preprint. Click to download.

- [Videoofdynamiccrackpropagationforufield.mp4](#)
- [VideoofdynamiccrackpropagationinFCNP.mp4](#)
- [Videoofdynamiccrackpropagationforvfield.mp4](#)